A Resistance Bridge Based on a Cryogenic Current Comparator Achieving Sub-10^{-9} Measurement Uncertainties

Wilfrid Poirier[ID], Dominique Leprat[ID], and Félicien Schopfer[ID]

Abstract—A new resistance bridge has been built at the Laboratoire national de métrologie et d'essais (LNE) to improve the ohm realization in the Système International (SI) of units from the quantum Hall effect. We describe the instrument, the performance of which relies on two synchronized and noise-filtered current sources, an accurate and stable current divider, and a cryogenic current comparator (CCC) having a low noise of 80 pA.t/Hz$^{1/2}$. The uncertainty budget for the measurement of the 100-$\Omega/(R_K/2)$ resistance ratio, where R_K is the von Klitzing constant, amounts to a few parts in 10^{10} only.

Index Terms—Bridge, cryogenic current comparator (CCC), metrology, quantum Hall effect, resistance, Superconducting QUantum Interference Device (SQUID).

I. INTRODUCTION

IN THE Système International (SI) [1], the ohm can be realized from $R_K = h/e^2$ [2], where h is the Planck constant and e is the elementary charge, using the quantum Hall effect. In national metrology institutes (NMIs), the quantized Hall resistance R_K/i, where i is an integer, is used as a universal primary reference to disseminate the ohm by means of resistance comparisons [3]. Performing these resistance comparisons is challenging since the measurement current of the quantum Hall resistance (QHR) devices must remain small, i.e., a few tens of μA, if based on GaAs/AlGaAs heterostructure [4], [5], and a few hundreds of μA, if based on graphene [6]. The most accurate and sensitive resistance bridge (RB), based on the performance of a cryogenic current comparator (CCC), is able to achieve relative measurements uncertainties of a few 10^{-9}. The CCC [7] is basically a perfect transformer operating in direct current regime (dc) able to measure the ratio of the currents circulating through the two resistances to compare with a relative uncertainty below 10^{-10}. Made of superconducting windings embedded in a superconducting shielding, its accuracy relies on the Meissner effect. Its high current sensitivity comes from the flux detector equipping it, which is based on a Superconducting QUantum Interference Device (SQUID) [8].

The development of RB equipped with a CCC started in several NMIs, including the French institute, right after the discovery of the QHE. First ones were equipped with radio frequency (rf) SQUID and used with dc [9]–[12]. The Laboratoire national de métrologie et d'essais (LNE) has been using such a dc bridge [9], [13] for more than 30 years to perform calibrations of wire resistors with a relative measurement uncertainty of a few 10^{-9}, as more than twenty NMIs do at the present time. Other bridges adapted to measurements in the low-frequency (below 1 Hz) alternating current regime (ac) were then proposed [14], [15]. Accurate operation at higher frequencies was achieved by replacing the CCC with a room-temperature current comparator using high-permeability magnetic cores [16], [17] but at the expense of larger measurement uncertainties. The improvement of digital and analog electronic components and the availability of dc SQUIDs then allowed several NMIs to develop RBs with better performance in terms of sensitivity, accuracy, and automation [18]–[21]. Despite this, achieving a combined measurement uncertainty below 10^{-9} remains very challenging. Among the NMIs having participated in the International bilateral comparisons [22] with the Bureau International des Poids et Mesures (BIPM), which are considered as giving one of the best validation of measurement uncertainty budgets, only three have reported on such low measurement uncertainties.

Here, we report on a new RB based on dc SQUID designed to perform comparisons of resistances over a wider range of values (from 1 Ω to 1.29 MΩ) and with lower measurement uncertainties than with the older bridge. Our estimated combined standard uncertainty for the measurement of the 100-$\Omega/(R_K/2)$ ratio amounts to 0.6×10^{-9} (1σ) only, in relative value. The type A relative uncertainty achieved for 1-h measurement can be as low as 0.2×10^{-9}. This compares with the five times larger uncertainty obtained with the older bridge due to the outdated performance of its rf SQUID.

II. PRINCIPLE OF THE RB

The principle of the new RB, described in Fig. 1, is close to that of the older one. It is based on two synchronized sources, primary (P) and secondary (S) sources, that deliver currents I_P and I_S, respectively. The primary (secondary) source supplies the resistance R_P (R_S) in series with a superconducting winding of a CCC of the number of turns N_P (N_S). N_S and N_P, are chosen so that the ratio N_S/N_P is close to the resistance ratio R_S/R_P. A standard current divider (SCD) is used to deviate
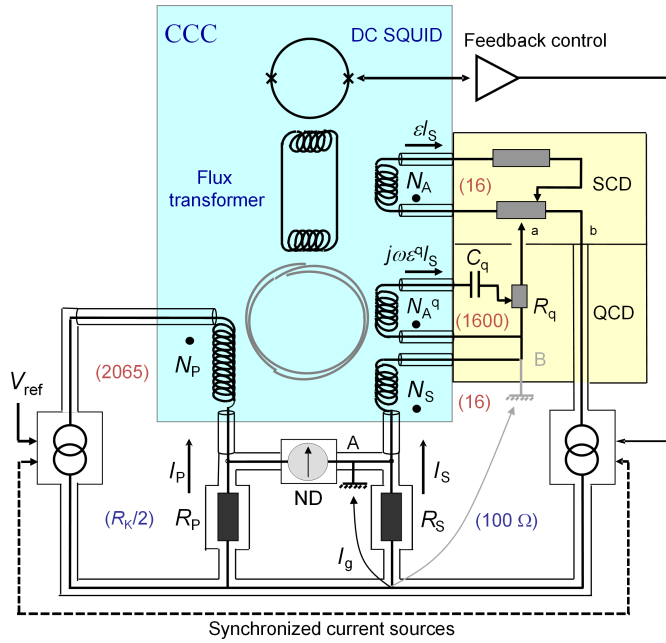
Fig. 1. Principle of the new LNE RB based on a CCC. The figure shows the two synchronized current sources, the CCC equipped with a dc SQUID and the feedback control on the secondary current source, the standard (SCD) and the quadrature (QCD) current dividers, the ND, and the two resistances R_S and R_P to compare. The ground can be connected in position A (low potential of the secondary resistor) or B (low potential of the secondary winding).

an in-phase calibrated fraction ϵ of the current I_S into an auxiliary winding of the number of turns N_A. The windings of the CCC are wound according to a toroidal geometry and embedded in a superconducting shielding. Application of the Ampere's theorem to a circulation along a cross section of the shielding, where the magnetic flux density is zero, leads to the relationship $N_P I_P - (N_S + \epsilon N_A) I_S = I_{CCC}$, where I_{CCC} is a screening current. Because the CCC shielding overlaps itself without electrical contact, this superconducting current circulates from the inner to the outer side of the shielding. It is detected by a pickup coil coupled to the outer side and connected to the entry inductance of a dc SQUID. The secondary current source is servocontrolled by the output of the CCC SQUID electronics so that the screening current I_{CCC} (i.e., the total ampere-turn) is nulled. It results in that

$$N_P I_P - (N_S + \epsilon N_A) I_S = 0. \tag{1}$$

From the fraction ϵ_{eq} setting the voltage balance (equilibrium), $R_S I_S = R_P I_P$, one obtains

$$R_S / R_P = (N_S + \epsilon_{eq} N_A) / N_P. \tag{2}$$

The SCD can also be inserted in the primary circuit to deviate a fraction of the current I_P. In this case, the previous equations remain valid by simply exchanging S and P indexes. This is the operating mode planned for measurements involving a low resistance R_S (for example, 1 Ω) supplied by a large current I_S (for example, 50 mA), which would lead to a too strong dissipation in the SCD if placed in the secondary circuit. Instead, the SCD inserted in the primary circuit is biased by the lower current I_P, which is usually below 10 mA.

Compared with the older RB, main improvements implemented in the new bridge concern: 1) the two current sources that are carefully noise-filtered and finely synchronized by a single external voltage source so that they are able to operate both in dc (in fact, a square current signal with periodic current reversal) and in ac (a sinusoidal current signal) at very low frequencies; 2) the new dc SQUID-based CCC that is equipped with more windings and is characterized by a lower noise level; 3) the SCD that is more accurate and stable; 4) the shielding that has better continuity and contributes to lower noise and better accuracy; and 5) the addition of a quadrature current divider (QCD) used to cancel the voltage overshoots (or in-quadrature signal) caused by stray capacitances that occur at the entry of the null detector (ND) during current reversals (or ac current variation).

Voltage overshoots, which become large for short current rise time, can lead to saturation of the ND during current transitions. To avoid this, one can adopt long enough current rise time and large filter time constant for the ND. However, this limits the current reversal frequency that is not favorable to offset subtraction and rejection of the $1/f$ SQUID noise. Moreover, this reduces the data acquisition time. The QCD offers an alternative solution applicable both in the dc regime and in the low-frequency ac regime. This new device can deviate an in-quadrature current fraction $j\omega\epsilon^q I_S$ in a fourth winding of number of turns N_A^q, where ω is the angular frequency, $\epsilon^q = \alpha R_q C_q$, and $\alpha \in [0:1]$ is a fraction adjusted by a potentiometer (see Fig. 1). Equation (1) for ampere-turns becomes

$$N_P I_P - (N_S + \epsilon N_A + j\omega\epsilon^q N_A^q) I_S = 0. \tag{3}$$

Considering stray capacitances C_P and C_S in parallel to the resistors R_P and R_S, respectively, and assuming first-order approximation in ω, the voltage balance is achieved provided that the fraction ϵ_{eq} obeys (2) and that the fraction ϵ_{eq}^q fulfills the following equation (see Appendix C-B):

$$(R_P C_P - R_S C_S)\omega = \epsilon_{eq}^q \omega \frac{N_A^q}{(N_S + \epsilon_{eq} N_A)} \simeq \epsilon_{eq}^q \omega \frac{N_A^q}{N_S}. \tag{4}$$

This equation emphasizes that the in-quadrature voltage signal due to stray capacitances can be compensated by the injection of the in-quadrature current, for any angular frequency ω, by setting the QCD fraction to the value $\epsilon_{eq}^q = \alpha_{eq} R_q C_q$. In dc operation of the bridge, the QCD allows the cancellation of the in-quadrature signals at the harmonic frequencies of the current reversal frequency, which form the parasitic voltage overshoots. One can, therefore, decrease the ND filter time constant and the current rise time and also increase the current reversal frequency without any risk of saturation of the ND. This allows reducing the impact of the voltage offset drift and of the $1/f$ SQUID noise on measurements and increasing the ratio between the acquisition time and the total experience time. Let us remark that the calibration of the QCD fraction is not required.
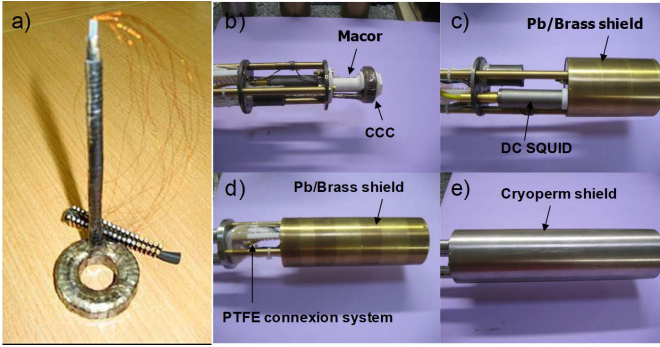
Fig. 2. Pictures of the CCC at different stages of shielding assembly. (a) CCC alone: the outer diameter, the inner diameter, and the height of the CCC are 42, 19, and 12 mm, respectively. The length of the chimney is 110 mm. (b) CCC on the probe with all shields removed. An additional superconducting cylindrical piece (length of 40 mm) extends the shielding of the chimney exit wires. (c) First Pb/Brass shield (length/diameter: 88 mm/60 mm) in place. (d) Second Pb/Brass shield (length/diameter: 180 mm/64 mm) in place. (e) External cryoperm shield (length/diameter: 256 mm/68 mm) in place.

III. CCC

A. Design and Fabrication

The CCC, as shown in Fig. 2(a), is made of 15 windings of 1, 1, 2, 4, 16, 16, 32, 64, 128, 160, 160, 1600, 1600, 2065, and 2065 turns that are held together with epoxy glue [23]. Each winding is made of superconducting and insulated 60-μm-diameter NbTi/Cu wire. We used optically checked 0.1-mm-thick Pb sheets and Pb/Sn/Cd superconducting solder at a temperature lower than the Pb melting temperature (~150 °C) to realize the toroidal shielding around the windings. Our shield overlaps twice (three layers) to prevent flux leakage. Each layer is covered with polytetrafluoroethylene (PTFE) tape for electrical insulation. The CCC is fixed to the cryogenic probe with a piece in Macor[1] material [see Fig. 2(b)]. The dc SQUID (Quantum Design, Inc.) has an input inductance of $L_i = 1.8$ μH and a nominal flux noise in flux-lock feedback mode of 3 $\mu\phi_0/\mathrm{Hz}^{1/2}$ above 0.3 Hz. It is coupled to the CCC via a superconducting flux transformer made of an NbTi wire inserted in a lead tube. Due to geometrical constraints, the number of turns of the pickup coil was reduced to $N_{\mathrm{PC}} = 6$. The magnetic screen is made of five concentric cylinders: two Pb ones, each one embedded in a brass one [see Fig. 2(c) and (d)], and an outer Cryoperm cylinder [see Fig. 2(e)]. Each cylinder is closed at the top with the same material. The cryogenic probe body is made of three rods used to stabilize it mechanically and reduce the CCC vibrations that cause electrical noise in measurements.

From the SQUID sensitivity, the N_{PC} number of turns, the SQUID input inductance L_i, and the effective CCC self-inductance, $L_{\mathrm{CCC}}^{\mathrm{eff}} \sim 14$ nH, determined taking into account the proximity of the superconducting screen [24], [25], one can calculate (see Appendix A) an expected CCC sensitivity S_{CCC} of 6 μA.t/ϕ_0. This value is close to that measured experimentally, $S_{\mathrm{CCC}} = 8$ μA.t/ϕ_0.
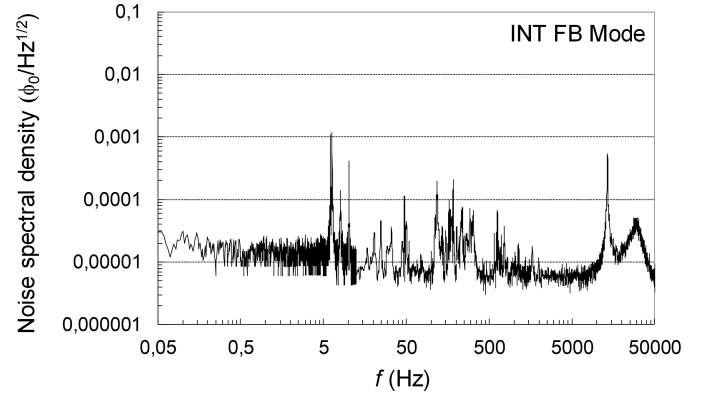
[1]Registered trademark.

Fig. 3. Noise spectral density measured by the SQUID, operating in internal feedback mode (mode 5), versus frequency f for the CCC alone (no external cable connected to any winding).

B. Noise Performance

The CCC was first tested with all windings disconnected (no external cable connected at room temperature). Fig. 3 shows the noise spectral density in $\phi_0/\mathrm{Hz}^{1/2}$, measured by the SQUID operating in internal feedback mode (through the modulation coil of the SQUID) as a function of the frequency. The main frequency resonance due to the coupling of the large inductance of windings and the capacitance between wires is around 14 kHz. Between 6 Hz and about 2 kHz, the noise spectral density is dominated by sharp peaks with an amplitude lower than 1 m$\phi_0/\mathrm{Hz}^{1/2}$, which are caused by mechanical resonances. At lower frequencies down to about 0.1 Hz, there exists a white noise regime with a constant noise spectral density of about 10 $\mu\phi_0/\mathrm{Hz}^{1/2}$. Considering the CCC sensitivity of 8 μA.t/ϕ_0, this leads to a current sensitivity of about 80 pA.t/$\mathrm{Hz}^{1/2}$, which is fifteen times better than the 1300-pA.t/$\mathrm{Hz}^{1/2}$ current sensitivity of the rf SQUID-based CCC of the older bridge. At frequencies lower than 0.1 Hz, one can observe a noise increase that can be explained by the $1/f$ noise of the Quantum Design dc SQUID. The operation of the RB with a current reversal frequency higher than 0.1 Hz should, therefore, lead to the lowest measurement noise.

C. Accuracy

Accuracy errors of the CCC are generally caused by a magnetic flux leakage that couples with the pickup coil [4], [26]. They can be detected by supplying windings of the same nominal number of turns N connected in series opposition with a large current I (= 100 mA, whatever N value) and measuring the magnetic flux δ_{ϕ_0} detected by the SQUID (operating in internal feedback mode). One then obtains the relative error $\Delta N/N = \delta_{\phi_0} S_{\mathrm{CCC}}/(NI)$, where NI/S_{CCC} should be the total flux generated by one winding (see results in Table I). A low-noise current source is required for these measurements to reduce the SQUID errors caused by noise rectification. Best measurements were obtained using the current source of the RB (see Section VII-A and Fig. 11), which is characterized by a small frequency bandwidth of 1 kHz and is equipped with homemade common-mode torus reducing the circulation of

TABLE I

RELATIVE ERRORS WITH STANDARD UNCERTAINTIES ($k = 1$) OF THE NUMBER OF TURNS, $\Delta N/N$, DETERMINED FROM WINDING OPPOSITION FOR DIFFERENT COMBINATIONS OF NUMBER OF TURNS

| Winding combination	$\Delta N/N$
1-1	$(1.29 \pm 0.38) \times 10^{-9}$
2-2	$(4.64 \pm 0.63) \times 10^{-10}$
16-16	$(1.9 \pm 1.2) \times 10^{-11}$
16+16-32	$(2.5 \pm 1.1) \times 10^{-11}$
16+16+32-64	$(0.22 \pm 0.76) \times 10^{-11}$
16+16+32+64-128	$(1.0 \pm 1.1) \times 10^{-11}$
160-160	$(2.5 \pm 0.14) \times 10^{-11}$
160-128-32	$(0.5 \pm 0.4) \times 10^{-11}$
1600-1600	$(5.6 \pm 0.032) \times 10^{-11}$
2065-2065	$(2.54 \pm 0.035) \times 10^{-11}$

Fig. 4. Schematics of the electronic circuits of primary and secondary current sources. Both current sources are controlled by a single external voltage source.

noise from the ground (see Section IV-C). For turn numbers N equal to 16 and 2065 that are used in the calibration of a 100-Ω resistor in terms of $R_K/2$, $\Delta N/N$ is found to be equal to $(1.9 \pm 1.2) \times 10^{-11}$ and $(2.5 \pm 0.04) \times 10^{-11}$, respectively. For all other winding opposition, turn errors are found smaller than 6×10^{-11}, except for 1-1 and 2-2 combinations that seem let us conclude to significant errors of $\sim 1 \times 10^{-9}$ and $\sim 5 \times 10^{-10}$. One could explain this observation by a magnetic flux leakage from the wiring at the top of the chimney or a hole in the toroidal shield. However, the chimney is rather long, and its end is well screened. Besides, a hole would also lead to errors for series opposition of windings with a larger number of turns. Our interpretation is that these apparent larger errors are rather caused by spurious signals coming from residual noise rectification, which manifest themselves all the more as the total ampere-turn number is small, i.e., for 1-1 and 2-2 winding oppositions. Further reduction of the noise emitted by the current source in the 100 mA range (which is the noisiest range) is required to refine the determination of winding errors for small numbers of turns.

Our conclusion is that the CCC errors in the measurements of usual resistance ratios, which exploited mainly windings of the number of turns 2065, 1600, 160, and 16, are of a few 10^{-11} only. These small residual errors are of similar magnitudes to those reported by other NMIs [22]. The CCC contribution to the type-B uncertainty, u_B^{CCC}, is, therefore, below 10^{-10}, in relative value.

IV. CURRENT SOURCE ELECTRONICS

A. Design

The RB is based on two current sources generating the currents I_P and I_S that supply the resistors R_P and R_S, respectively. In some recently developed RBs, current sources are based on digital electronics connected by fiber optics to an internal microcontroller [19], [21] or an external PXI computer. This provides strong electrical insulation and easy automation but requires the implementation of efficient noise filtering techniques to protect the SQUID from the rf noise emitted by digital circuits.

On the contrary, current sources of the new LNE RB remain based on linear analog circuits to avoid high-frequency noise [23]. Fig. 4 shows the schematic of the two electronic circuits,
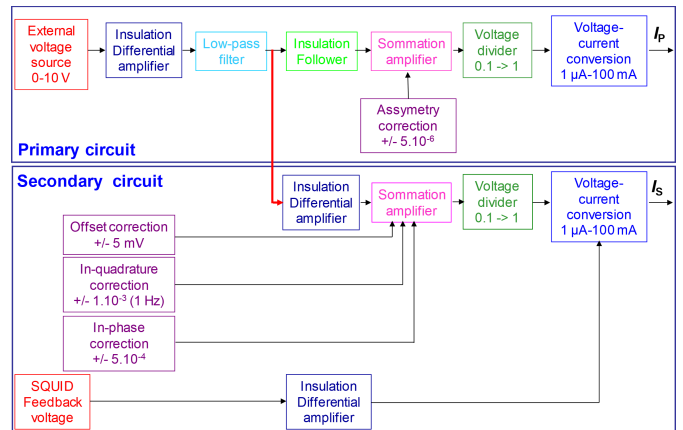
the primary and the secondary ones. They are controlled and synchronized by a single external voltage source, allowing automation of measurements. The latter can be either a dc voltage generator, such as a Yogogawa 7651 for usual dc measurements or the oscillator of a lock-in detector for low-frequency ac measurements. The external reference voltage supplies the primary circuit through a high-impedance differential amplifier. A low-pass filter is then used to limit the signal bandwidth with an adjustable cutoff frequency ranging from 1 mHz to 1 kHz. After a stage summing additional voltage corrections and a division stage allowing the setting of a decimal fraction, the voltage is converted into a current in ranges extending from 1 μA up to 100 mA. This conversion is done using an amplifier inverter circuit boosted by a buffer amplifier (BUF634T) and a dividing resistor R_C (see Fig. 6). The secondary current source, controlled by the output signal of the low-pass filter of the primary current source, is similar, but the current range selected can also be multiplied by a factor 1.2906 or 1/1.2906 to adapt to the measurement of the specific resistance ratios involving the QHR connected either to the primary or to the secondary current sources. Besides, the design is such that there is no common-mode voltage between the primary and secondary circuits (the 0-V references of the two circuits, although electrically isolated, are at the same potential by design), which is beneficial to adjust the current ratio. Nevertheless, several additional circuits are required to finely adjust the current ratio $r_I = I_S/I_P$ to within a few parts in 10^6 prior to the SQUID feedback operation. This is necessary to limit the ampere-turn unbalance in the CCC, not only to avoid unlocking of the SQUID feedback notably during current switching but also to achieve the best accuracy in the I_S/I_P ratio adjustment. Offset, in-phase, and in-quadrature correction circuits are used to tune the secondary current. An asymmetry correction circuit, which corrects the main voltage by a small fraction of its absolute value, is also used in the primary circuit. It compensates for, to some extent (to within a few 10^{-7}), the asymmetry behavior of the electronic circuits, which manifests by a small change of the current ratio (typically 2×10^{-6} in relative value) when reversing the current. Finally, the SQUID feedback
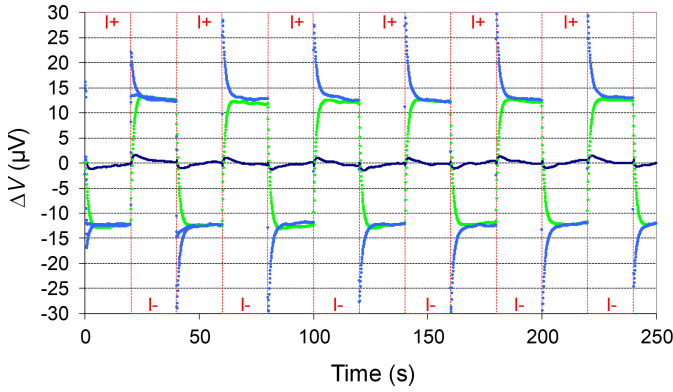
Fig. 5. Illustration of the adjustability of the current ratio I_P/I_S using resistances $R_P = 10$ kΩ and $R_S = 100$ Ω (the SQUID feedback control is not operating). The balance voltage ΔV, measured by the ND, is recorded as a function of time, while the current is periodically reversed (red dashed line) for different settings of the corrections circuits: adjustment of the offset correction only (blue line), adjustment of the in-quadrature correction (green line), and adjustment of in-phase, in-quadrature, and asymmetry corrections (deep blue line).
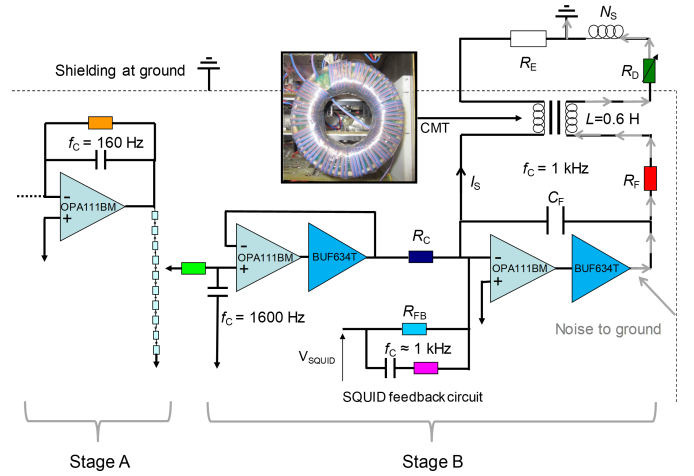

Fig. 6. Electronic schematic of the two last stages (A and B) of the secondary current source (the primary current source does not include the SQUID feedback circuit) describing the noise filtering techniques. Picture of the CMT used to block the circulation of current noise toward the ground (an example is shown with gray arrows). The dotted line represents the limit of the case (at ground) of the current source.

voltage, after insulation using another high-impedance differential amplifier, is converted into a feedback current at the last stage of the secondary circuit so that the external feedback through the CCC winding has the same closed-loop gain as in the internal feedback mode, i.e., ~ 0.75 V/ϕ_0.

Electronic circuits of current sources are made of precision operational amplifiers and high-stability and low-temperature coefficient Vishay resistors. They are carefully shielded and electrically isolated from the ground (see Appendix B-A).

B. Test of the Current Ratio Adjustability

Fig. 5 shows the experiment carried out to test the adjustability of the ratio of the two current sources, which can be achieved prior to operating the SQUID feedback control [23]. Two resistors of resistance 10 kΩ and 100 Ω are fed by currents I_P and I_S, respectively. The potential drop difference ΔV at the terminals of the two resistors is recorded by an ND (nanovoltmeter EM N11). For a nominal voltage reversing from 1 to -1 V every 20 s, Fig. 5 shows that it is possible to reduce the peak-to-peak ΔV amplitude to less than 2 μV by adjusting the in-phase, in-quadrature, offset, and asymmetry corrections (the latter correction is used to symmetrize ΔV when reversing the current). Let us notably remark the effect of the in-quadrature correction in canceling the voltage overshoot caused by the fast current reversal. This experiment proves that the current ratio can be adjusted to within 2×10^{-6}, in relative value, even during a fast current reversal, which is an advantage both to avoid any SQUID unlocking and achieve the best accuracy (see Appendix D).

C. Noise Optimization and Filtering

Noise filtering is crucial particularly from the resonance frequency of the CCC (14 kHz) up to the operating frequency of the modulation circuit (500 kHz) not only to ensure a good working of the SQUID but also to avoid noise rectification that would alter measurement accuracy. Fig. 6 shows the last stage of the electronic circuit of the secondary current source that supplies the resistance under measurement, R_E, in series

with a CCC winding. The primary current source is based on a similar stage but differs by the absence of the SQUID feedback electronic circuit. In practice, the frequency bandwidth of the primary and secondary current sources was reduced to 160 Hz using a simple low-pass filter at stage A of the circuit. The filtered voltage is then converted into a current using the resistance R_C, the value of which defines the current range. A second low-pass filter with a cutoff frequency of 1 kHz, defined by the capacitance C_F and the resistances R_F, R_E and R_D (SCD resistance), is implemented at stage B to damp the CCC resonances. This filter limits the frequency bandwidth of the SQUID feedback circuit servocontrolling the secondary current to 1 kHz. The values of the passive components chosen for the different current ranges are given in Appendix B-B.

It is also essential to avoid the circulation of the current noise coming from the capacitive coupling of the electronics circuit with the ground. To cancel this noise source that renders the SQUID inoperative, a homemade common-mode torus (CMT) was introduced in the current circuit of each source (see Fig. 6). This CMT is made of a PTFE insulated wire pair wounded about 60 times around a magnetic nanocrystalline torus from Aperam (relative magnetic permeability of about 80 000 up to a 100-kHz frequency) with an antiprogression turn returning to the beginning of the winding [27]. The differential inductance is around 3 μH, while the common-mode inductance is around 0.6 H. The common-mode impedance, which increases from about 200 Ω at 50 Hz up to 150 kΩ at 1 MHz, drastically reduces the circulation of the common-mode current noise. This protects the SQUID and makes it operating quite ideally whether it is an rf or a dc SQUID.

D. SQUID Feedback Circuit

The Quantum Design SQUID can operate in four internal feedback operation modes, 5/5 s, 50, and 500 of closed-loop feedback gains 0.75 V/ϕ_0, 0.075 V/ϕ_0, and 0.0075 V/ϕ_0, respectively. These gains are defined by feedback resistors of

resistance values, 500, 50, and 5 kΩ, respectively, that divide the SQUID voltage detected after amplification by an integrator to generate the feedback current injected in the modulation coil. The SQUID bandwidth, defined by the characteristic frequency of the integrator amplifier (which defines the open-loop gain), is 50 kHz except for the 5 s mode for which it is reduced to 500 Hz. In external feedback mode, the feedback circuit is disconnected from the modulation coil, and the voltage signal, V_{SQUID}, detected at the output of the SQUID preamplifier, is sent to the secondary current source of the bridge after decoupling by a high-impedance differential amplifier. The SQUID feedback resistors, therefore, no more define the closed-loop gains. On the other hand, another resistor R_{FB} biased by the V_{SQUID} voltage is used to define the feedback current supplying the secondary winding (N_S). The resistor value, $R_{FB} = 1.5$ MΩ, is chosen so that the closed-loop feedback gain $G_{CLG} = R_{FB} \times S_{CCC}/N_S$ for $N_S = 16$ has the same value as in the most sensitive internal feedback mode of the SQUID (mode 5/5 s), i.e., 0.75 V/ϕ_0. For larger values of N_S, the voltage V_{SQUID} is reduced by a factor ($N_S/16$) using a voltage divider (not shown) to maintain G_{CLG} at the same value. The stability of the closed-loop feedback operation also requires that the feedback circuit generates small-signal dephasing. To partially compensate for the dephasing caused by the 1-kHz low-pass filter implemented in stage B of the electronic circuit and, therefore, optimize the SQUID operation, a circuit made of a small capacitance of 200 pF in series with a 20-kΩ resistor was connected in parallel to the 1.5-MΩ resistor.

V. CURRENT DIVIDERS

A. Standard (or In-Phase) Current Divider

The SCD is used to balance the dc (or in-phase) voltages measured at the terminals of the two resistors by deviating a fraction of current toward the auxiliary winding. This is a key element, the accuracy of which directly impacts the uncertainty budget of the RB. An alternative technique to null the voltage measured by the detector consists in using a calibrated auxiliary current source servocontrolled by the ND voltage output [10], [11]. On the contrary, the SCD developed is a passive component that avoids the use of a second feedback electronics and aims for good stability of all current fractions. This can be achieved with a design that limits the number of electrical commutations required to select the current fraction. The counterpart is that the calibration of the LNE SCD is not fully automated contrary to that of binary compensation units [28], [29].

Achieving a linear and stable SCD allowing the injection in the auxiliary winding of a fraction of the main current that ranges from 0 to 5×10^{-5} with a minimal step of 5×10^{-8} is a challenge. The SCD, described in Fig. 7, is made of three main series resistor networks (10×20, 10×2, and 10×200 Ω) and a large 4-MΩ division resistor. The nominal current fraction is given by: $\epsilon_{(N,P,Q)}^{nom} = N \times 5 \times 10^{-6} + P \times 5 \times 10^{-7} + Q \times 5 \times 10^{-8}$, where N, P, and Q are the integer values between 0 and 10 indexing the position of three selecting mechanical commutators (commutators with gold-coated silver contacts from I.E.C. Electronique).
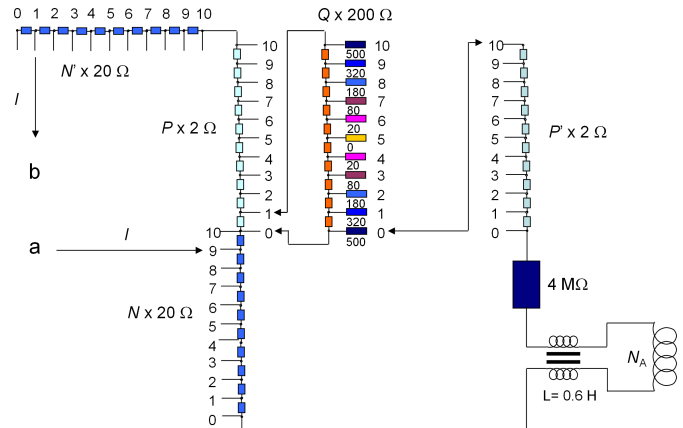

Fig. 7. Electrical schematic of the SCD. N, P, and Q are integers defining the setting of the SCD ($N' = 10 - N$ and $P' = 10 - P$). A CMT is inserted between the SCD and the auxiliary winding to reduce the current noise circulation through the ground. Connection points, a and b, are indicated in Fig. 1.

The SCD is designed so that the selection of a given fraction does not require the disconnection of any of the resistors forming the three main networks: they remain soldered. Besides, the definition points of the fractions in a network, indexed by an integer, are physically realized by soldered wires. Moreover, high-stability (drift lower than 10^{-5}/year, in relative value), low-temperature coefficient ($< 0.6 \times 10^{-6}/°C$), and hermetically shielded Vishay resistors are used. The maximum power is dissipated in the 20-Ω resistors and remains below 2 mW. All these technical considerations ensure better stability and reproducibility of the SCD, even under load. The counterpart of the design is that nonlinearities result from the variation of the P and Q parameters. Indeed, the triangle formed by resistors (2, $Q \times 200$, and $(10-Q) \times 200$ Ω) leads to the addition of a Q-dependent resistance to the 4-MΩ resistance. This nonlinearity is solved by adding a compensation resistance in series with the 4-MΩ resistance that is selected for each Q value among the resistor network (500, 320, 180, 80, 20, 0, 20, 80, 180, 320, 500 Ω). The division resistance defining the ratio also varies as a function of the P parameter. This is compensated by selecting a fraction of the resistor network (10×2 Ω) using the index $P'=10 - P$. Finally, the fraction of the resistor network (10×20 Ω) selected by N' index adds to keep constant the total resistance of the SCD, $R_D = 220$ Ω, independently of the N index change: $N'=10 - N$. This is useful to set the frequency bandwidth of the current source independently of the SCD setting. Let us note that a CMT is also introduced in the SCD circuit to reduce the current noise signals circulating from ground to the auxiliary winding (see the picture in Appendix C).

The usual calibration of the SCD consists in measuring the three following sets of fractions: (N, $P = 0$, and $Q = 0$), ($N = 0$, P, and $Q = 0$) and ($N = 0$, $P = 0$, and Q), with N, P, and Q varying from zero to ten. Any fraction is calibrated with a typical upper bound uncertainty of 3×10^{-10} (see Appendix C-A). Fig. 8 reports on the time evolution over ten years of the determined corrections that must be added to the nominal values for the three ranges of fractions.
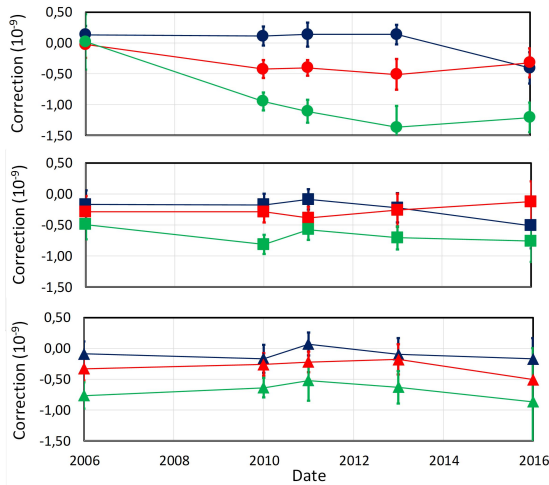
Fig. 8.   Time evolution over ten years of the corrections ($\epsilon_{N,P,Q} - \epsilon_{N,P,Q}^{\text{nom}}$), expressed in 10^{-9}, that must be added to the nominal fractions, ($N \times 5 \times 10^{-6}$) (circle), $P \times 5 \times 10^{-7}$ (square), and $Q \times 5 \times 10^{-8}$ (triangle) for three values of the integer index, 1 (blue), 5 (red), and 9 (green). Error bars correspond to standard uncertainties (1σ).

Fig. 9.   Left: picture of the RB. Right: picture of the CCC winding switching box at the top of the cryostat.

Calibrations show that the fractions have remained close to their nominal value within 10^{-9}, drifting each by no more than 5×10^{-10}, except for the highest one ($9 \times 5 \times 10^{-6}$), which has changed a bit more. The mean drift has been less than 1×10^{-10}/year between 2010 and 2016 (for future uses of the RB, the SCD will be calibrated every year). A fraction $\epsilon_{(N,P,Q)}$ is then obtained from four calibrated fractions by

$$\epsilon_{(N,P,Q)} = \epsilon_{(N,P=0,Q=0)} + \epsilon_{(N=0,P,Q=0)} \\ + \epsilon_{(N=0,P=0,Q)} - 2\epsilon_{(0,0,0)}. \quad (5)$$

Its uncertainty, $u_{\text{B}}^{\text{SCD}}$, is about 0.5×10^{-9}. For more accurate resistance measurements, as those performed for international comparisons, the $\epsilon_{(N,P,Q)}$ fractions used can be specifically calibrated to within an uncertainty of 0.35×10^{-9}.

B. Quadrature Current Divider

The QCD, connected in series with the SCD (see Fig. 1), injects an in-quadrature fraction $j\omega\epsilon^{\text{q}} = \alpha R_{\text{q}} C_{\text{q}} \omega$ of the main current in a CCC auxiliary winding of number of turns N_{A}^{q}, as highlighted by (3) and (4). More precisely, the main current is flowing through a R_{q} resistor. A 100-Ω potentiometer connected in parallel allows the adjustment of the voltage fraction α biasing a $C_{\text{q}} = 235$-nF PTFE capacitor (its parallel resistance is higher than 2×10^{13} Ω) in series with the CCC auxiliary winding. Depending on the amplitude of the quadrature compensation required, N_{A}^{q} is typically varied between 128 and 1600, and R_{q} is chosen equal to either 1 or 10 Ω (exceptionally 100 Ω). For the measurement of the 100-$\Omega/(R_{\text{K}}/2)$ ratio, usually $N_{\text{A}}^{\text{q}} = 160$ and $R_{\text{q}} = 1$ or 10 Ω. Prior to automatic measurements, the quadrature compensation is adjusted using the potentiometer so that the voltage overshoots observable during manual reversing of the current direction disappear. If the bridge is controlled by the ac signal of a
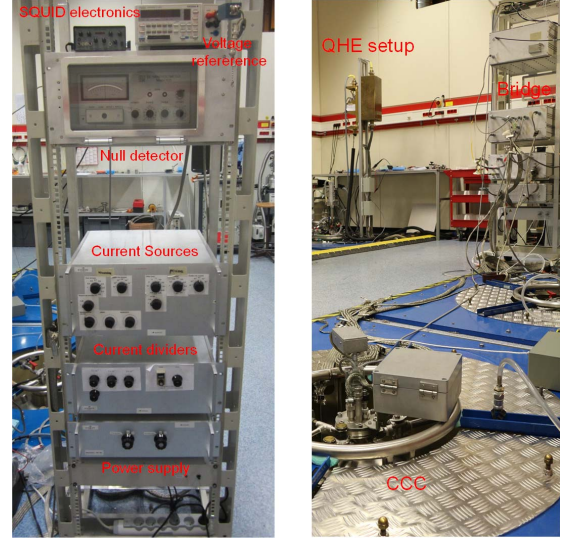
lock-in oscillator, the QCD is adjusted to cancel the quadrature voltage signal.

In dc operation of the bridge, it is crucial that the QCD does not inject any current during data recording (or any in-phase current in ac operation of the bridge). Considering a current rise time of 0.5 s in dc operation, one can calculate that the injected current fraction drops down to no more than a few 10^{-14} (10^{-13}) of the main current after a waiting time of only 8 s for $R_{\text{q}} = 1$ Ω ($R_{\text{q}} = 10$ Ω). For $N_{\text{A}} = 16$ and $N_{\text{A}}^{\text{q}} = 160$, the relative error on the resistance ratio caused by this residual current is ten times larger; however, it remains negligible ($u_{\text{B}}^{\text{QCD}} < 10^{-12}$ for $R_{\text{q}} = 1$ Ω). Let us note that the QCD is also equipped with a CMT to reduce the current noise circulation (see Fig. 16).

VI. Shielding and Guarding

To shield against noise, the sensitive elements of the RB (the ND, the current sources, the current dividers, and the power supply) were integrated into metallic boxes (see Fig. 9). Both with the QHR and the CCC setups, they are connected at the ground, which is materialized by the copper floor of the laboratory Faraday cage. The continuity of the shielding between the different elements is ensured by the connection cables, the metallic sheath of which is also connected at the ground, as schematized in Fig. 1. Cables are connected using shielded PTFE-insulated Fischer connectors. This directs any leakage current between wires at different potentials toward the ground. In normal operation, the ground is connected both to the low potential of the resistance R_{S} (position A in Fig. 1) and to the case of the EM detector (there is no common-mode voltage). The leakage current I_{g}, therefore, short-circuits the lowest resistance (black arrow in Fig. 1), which reduces its impact. This grounding is usually efficient to limit the leakage current contribution to the type B relative uncertainty below 10^{-9} for the measurement of the 100-$\Omega/(R_{\text{K}}/2)$ ratio. The ground can also be connected to the low potential of the

TABLE II
SETTINGS OF THE RB FOR SEVERAL RESISTANCE RATIO MEASUREMENTS

Ratio	N_P	N_S	N_A	SCD position
100 $\Omega/(R_K/2)$	2065	16	16	secondary source
200 $\Omega/(R_K/2)$	2065	32	16	secondary source
100 $\Omega/10$ kΩ	1600	16	16	secondary source
1 k$\Omega/(R_K/2)$	2065	160	160	secondary source
100 $\Omega/1$ kΩ	160	16	16	secondary source
1 k$\Omega/1$ kΩ	160	160	64	secondary source
10 k$\Omega/1$ MΩ	1600	16	16	secondary source
1 $\Omega/100$ Ω	1600	16	1600	primary source

Fig. 10. Noise spectral density measured by the SQUID versus frequency f for the measurement of the 100-Ω/10-kΩ ratio. SQUID operating in internal feedback mode 5 (black), in external feedback mode 5 s (red), and in external feedback mode 500 (blue).

secondary winding (position B in Fig. 1). The CMT remains efficient, and the SQUID operation stays optimal. In this case, the leakage current short-circuits both the resistor and the winding of the secondary circuit (gray arrow in Fig. 1) and, therefore, does not degrade the measurement accuracy.

Let us remark that the QCD adjustment depends on the ground point position since it changes the quadrature leakage current. Settings $R_q = 1$ Ω and $N_A^q = 128$ and 160 are generally adapted for ground in position B since the capacitance leakage current is fully deviated. As expected, larger values of R_q or N_A^q are required for ground in position A and $R_S \geq 1$ kΩ.

VII. RESISTANCE RATIO MEASUREMENTS

A. Noise Spectrum and SQUID Feedback Stability

The operation stability of the RB, i.e., of the SQUID, was demonstrated for the measurement of many resistance ratios. Table II presents the settings of the RB, which were used for the measurements reported in this article.

Here, we focus on the analysis of the noise spectral density, expressed in $\phi_0/\text{Hz}^{1/2}$, determined by the Quantum Design SQUID operating in different internal and external feedback modes for the measurement of the 10-kΩ/1-MΩ, 100-Ω/10-kΩ, and 1-Ω/100-Ω ratios (the quadrature divider was not used for these tests).

Fig. 10 shows the noise spectral density obtained for the measurement of the 100-Ω/10-kΩ ratio using 10-mA/100-μA current ranges. In closed-feedback mode operation, the measured noise corresponds to the uncorrelated noise contributions of both current sources since the current ratio I_S/I_P is adjusted to within 2×10^{-6} to cancel the ampere-turn unbalance of the CCC, i.e., the magnetic flux in the SQUID. Let us note that the residual magnetic flux noise crossing the SQUID itself has a much lower level because of the real-time compensation by the feedback signal. It is given by the combination of the intrinsic SQUID noise (3 $\mu\phi_0/\text{Hz}^{1/2}$), the environmental noise directly captured by the SQUID, and the current source noise divided by the open-loop amplification gain. This latter contribution is negligible. The two others, which manifest in the CCC alone and disconnected, give a contribution of about 10 $\mu\phi_0/\text{Hz}^{1/2}$, as shown in Fig. 3.

In the internal feedback mode 5, the SQUID open-loop bandwidth of 50 kHz allows measuring the noise level up to the frequency resonances of the CCC. The noise amplitude is above a noise floor level of about 140 $\mu\phi_0/\text{Hz}^{1/2}$. This
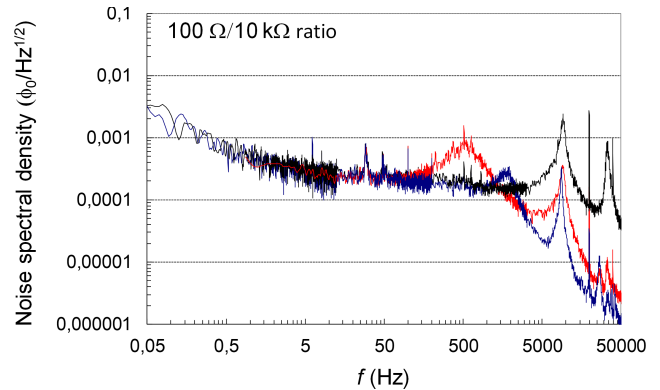
bottom level is notably explained by the Johnson–Nyquist noise, of 120 $\mu\phi_0/\text{Hz}^{1/2}$, generated by the $R_C = 50$-kΩ resistor defining the 100-μA current range of the primary current source. Below 10 Hz, the noise increase is mainly caused by the $1/f$ voltage noise of the operational amplifiers (OPA111BM) that drive the R_C resistor. The operation in external feedback mode 5 s is very stable. As can be observed, the noise spectrum is similar but is characterized by a lower frequency bandwidth limited to about 500 Hz, which manifests itself by a small peak above which the signal then decreases of 20 dB by decade. This can be explained by the reduction to 500 Hz of the SQUID open-loop bandwidth, which is recommended to improve the stability in the presence of short electromagnetic transients and the 1-kHz frequency bandwidth of the feedback circuit (see Section IV-D). The operation in the external feedback mode 500 also turns out to be stable. It is characterized by a noise spectrum having a higher cutoff frequency of about 1 kHz determined by the feedback circuit only (the SQUID open-loop bandwidth is of 50 kHz). In some measurement configurations, this larger frequency bandwidth can improve the stability of the bridge operation against acoustic noises. However, generally, the bridge is operated using the external feedback mode 5 s.

Fig. 11(a) and (b) demonstrates the stability of operation of the external SQUID feedback in the measurements of the 1-Ω/100-Ω and 10-kΩ/1-MΩ ratios, respectively. The base noise level is larger for the measurement of the 1-Ω/100-Ω ratio (above 2 m$\phi_0/\text{Hz}^{1/2}$). This comes from the reduction to 5 kΩ of the resistor R_C defining the 1 mA range used to supply the 100-Ω resistor. Conversely, the current sources are feebly noisy in the measurement configuration of the 10-kΩ/1-MΩ ratio because of the $R_C = 5$-MΩ resistor defining the 1-μA range. One can observe in Fig. 11(b) a white noise level of no more than 20 $\mu\phi_0/\text{Hz}^{1/2}$ between 0.2 Hz and 6 Hz. This low base noise level allows observing the manifestation of moderate mechanical resonances in the range from 10 Hz to 1 kHz.

B. Measurement Protocol and Type A Uncertainty

Measurements of the resistance ratio $r_R = 100$ $\Omega/(R_K/2)$ were performed using the old and the new LNE bridges. The
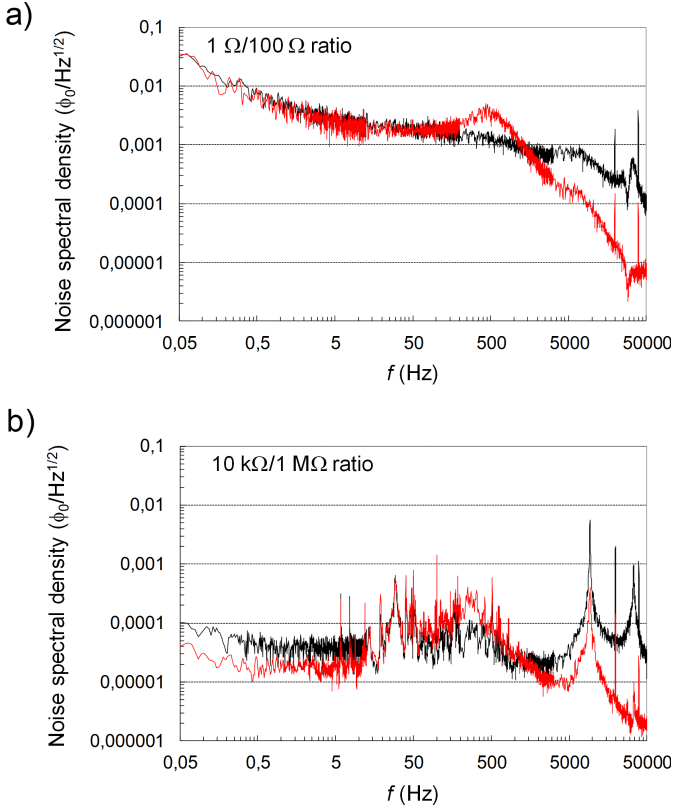
a)

b)

Fig. 11. Noise spectral density measured by the SQUID versus frequency f for the measurement of (a) 1-Ω/100-Ω ratio and (b) 10-kΩ/1-MΩ ratio. SQUID operating in internal feedback mode 5 (black) and in external feedback mode 5 s (red).

a)

b)

Fig. 12. Measurement of the resistance ratio $r_R = 100\ \Omega/(R_K/2)$ using the (a) old and (b) new LNE bridges with a primary current $I_P = 70\ \mu$A: relative voltage deviation $\Delta V/V$ as a function of time for several (I^+, 0, and I^-) sequences. The signal period is about 200 s. Insets: enlargement of voltage plateaus. The following settings were used: $N_P = 1936$, $N_S = 15$, and $N_A = 15$ for the older bridge and $N_P = 2065$, $N_S = 16$, $N_A = 16$, $N_A^q = 160$ and $R_q = 10\ \Omega$ for the new bridge. ϵ fractions are chosen to obtain similar deviation amplitude, $\Delta V/V$, for both bridges. ϵ^q setting of the new bridge QCD is optimized to cancel overshoots occurring during current reversals.

primary current circulating through the GaAs/AlGaAs-based quantum resistance standard is set to $I_P = 70\ \mu$A. For a ϵ fraction of the SCD that differs from ϵ_{eq} (giving $\Delta V = 0$), a finite voltage ΔV can be detected by the ND. For all resistance comparisons reported in this article, the voltage ΔV is measured by an EMN 11 nanovoltmeter (1.3 s time constant and 3-μV range), the isolated output of which is recorded by a $6^{1/2}$ digit Keithley 2000 multimeter (sample rate of 4 Hz). The relative voltage $\Delta V/V$, where $V = R_P I_P$, is related, at the first order, to the deviation ($\epsilon - \epsilon_{eq}$) by

$$\Delta V/V = (\epsilon - \epsilon_{eq}) \frac{N_A}{N_S}. \tag{6}$$

Let us note that, reversely, $\Delta V/V$ could be interpreted as a relative deviation of the ratio r_R to the value $r_{R_{eq}}$ giving $\Delta V = 0$ for the fraction ϵ. $\Delta V/V$ measured as a function of time during several (I^+, 0, I^-) sequences is reported in Fig. 12(a) and (b) for the old and the new LNE bridges, respectively. The signal period, of about 200 s, is imposed by the low-speed capability of the older bridge. The comparison of both data first shows the lower noise level and better stability achieved in measurements performed with the new bridge. This comes not only from the better performance of the current source electronics but also from the lower noise level of the CCC. Second, it demonstrates the efficiency of the QCD in canceling any voltage overshoot during the current switchings. This allows
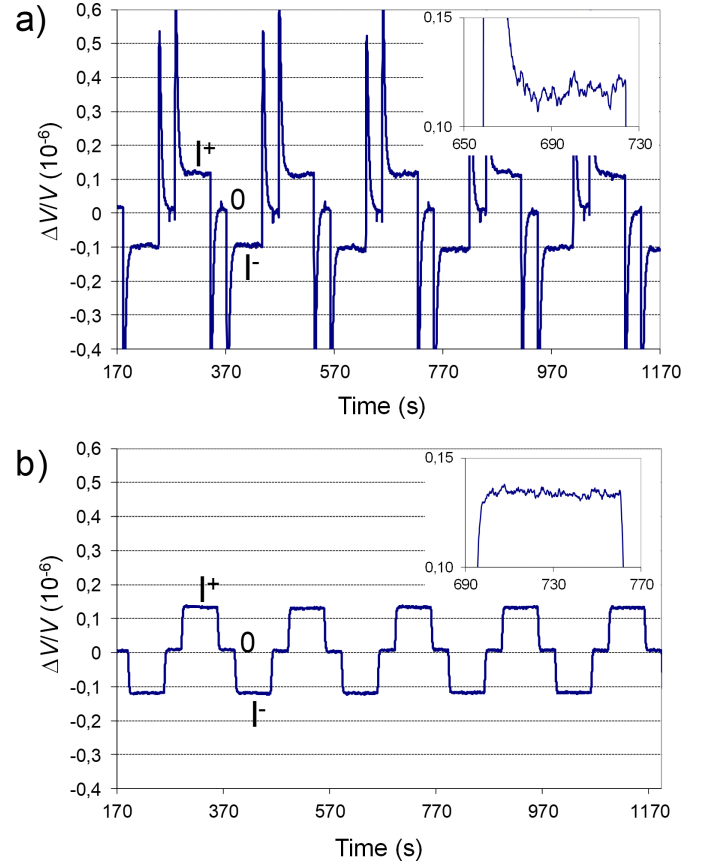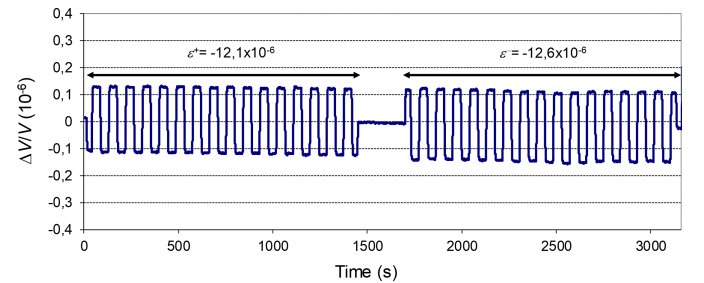

Fig. 13. Measurement of the resistance ratio $r_R = 100\ \Omega/(R_K/2)$, using the new LNE bridge with a primary current $I_P = 70\ \mu$A: relative deviation $\Delta V/V$ as a function of time for 16 (I^+, I^-, and I^+) sequences and two successive settings, $\epsilon^+ = -12.1 \times 10^{-6}$ and $\epsilon^- = -12.6 \times 10^{-6}$, of the SCD fractions.

increasing the current reversal frequency in order to reduce the impact of the voltage offset drift and the $1/f$ SQUID noise.

Fig. 13 shows the typical data record adopted for the measurement of the resistance ratio $r_R = 100\ \Omega/(R_K/2)$ with the new bridge. It consists of two successive acquisitions of voltage measurements that are obtained for the two settings of the SCD fractions, $\epsilon^+ = -12.1 \times 10^{-6}$ and $\epsilon^- = -12.6 \times 10^{-6}$,
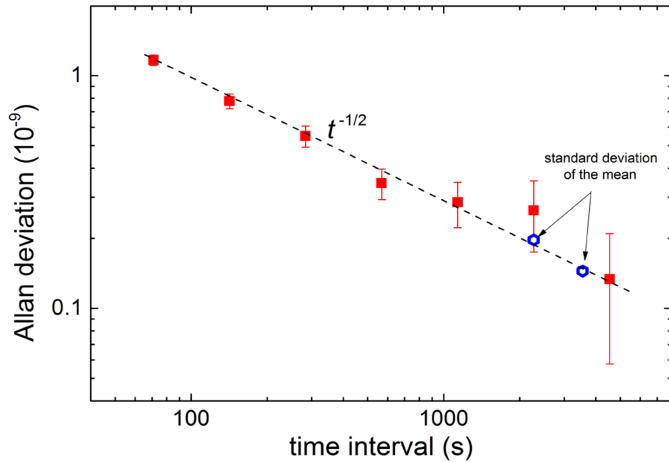
Fig. 14. Measurement of the resistance ratio, $r_R = 100~\Omega/(R_K/2)$, using the new LNE bridge with a primary current $I_P = 50~\mu$A and a signal period of 70 s. From an experiment described in supplementary of [6]. Standard Allan deviation of r_R, expressed in relative value, as a function of the acquisition time t (red square). $t^{-1/2}$ adjustment of data (black dashed line). Standard deviation of the mean (blue open hexagon).

TABLE III
PRELIMINARY RELATIVE UNCERTAINTY BUDGET FOR THE 100-$\Omega/(R_K/2)$
RATIO CONSIDERING A $I_P = 50$-μA MEASUREMENT CURRENT

Contributions	Name	Contributions (10^{-9}, k=1)
Type A (1 hour)	u_A	**0.15**
Type B	u_B	**0.7 (A), 0.5 (B)**
CCC accuracy	u_B^{CCC}	< 0.1
SQUID feedback accuracy	u_B^{FB}	< 0.01
SCD calibration	u_B^{SCD}	< 0.5
QCD	u_B^{QCD}	< 0.001
Leakage to ground	u_B^g	∼ 0.5 (A), 0.1 (B)
Combined Uncertainty	u_c	**0.7 (A), 0.6 (B)**

respectively. Each acquisition is made of 16 (I^+, I^-, and I^+) sequences of current reversal that is used to remove voltage offsets. The current rise time and the waiting time before acquisition are set to 0.5 and 12 s, respectively. A mean voltage value is calculated from the average of the 16 values $[V(I^+)_1 + V(I^+)_3 - 2V(I^-)_2]/4$, where $j = 1, 2$, and 3 indexes the current state of each sequence and $V(I^\pm)_j$ is itself the mean value of 60 voltage measurements. The resistance ratio is then obtained from the ϵ_{eq} value calculated from the two mean voltages, V^{ϵ^-} and V^{ϵ^+}, using the relation

$$\epsilon_{eq} = \epsilon^- + (\epsilon^+ - \epsilon^-) \times \frac{|V^{\epsilon^-}|}{(|V^{\epsilon^-}| + |V^{\epsilon^+}|)}. \qquad (7)$$

Due to the new bridge performances, the period of the signal was, therefore, reduced to about 70 s, and the zero-crossing step was removed. The result is that the ratio between the acquisition time and the total experiment time is increased from about 50% with the older bridge to 75% with the new bridge, which is favorable to a reduction of the type A uncertainty. Similar operation of the new RB is achieved for the measurement of other ratios using the settings reported in Table II and adapted QCD adjustments: 200 $\Omega/(R_K/2)$, 100 $\Omega/10$ kΩ, 1 k$\Omega/1$ kΩ, and 100 $\Omega/1$ kΩ.

The noise performance of the new LNE bridge is demonstrated by the calculation of the Allan standard deviation [30], [31] of $r_R = 100~\Omega/(R_K/2)$ from the statistical analysis of the voltage measurements performed using a primary current $I_P = 50~\mu$A. The evolution of this quantity, expressed in relative value, is reported in Fig. 14 as a function of the experience time t. It follows a $t^{-1/2}$ law over measuring times longer than 1 h. This shows that the white noise is dominant and that the standard deviation of the mean can be used as an estimate of the type A relative uncertainty, u_A. It follows that $u_A = 0.15 \times 10^{-9}$ can be achieved for the measurement of the ratio $r_R = 100~\Omega/(R_K/2)$ using a current of 50 μA after an observation time of 1 h. This is five times less than the best

uncertainty achievable with the older bridge. This improvement relies not only on the quicker measurement protocol but also on the lower noise of the current source electronics and of the CCC. Let us remark that the contribution of the CCC to the voltage noise at the terminals of the ND is no more than 0.5 nV/Hz$^{1/2}$. This is more than ten times lower than the EM N11 nanovoltmeter contribution, of about 7 nV/Hz$^{1/2}$, which clearly limits the bridge type A uncertainty. Considering a ratio of 75% between the acquisition time and the total experiment time, its noise leads to a calculated type A relative uncertainty of $1.15 \times 10^{-8} t^{-1/2}$ in good agreement with the Allan deviation reported in Fig. 14.

C. Uncertainty Budget

Table III itemizes the uncertainty budget established for the measurement of the 100-$\Omega/(R_K/2)$ ratio. The Type A and Type B contributions related to CCC accuracy, SCD calibration, and QCD have already been discussed. Below are considered other Type B contributions, including those caused by SQUID feedback and leakage current.

1) SQUID Feedback Accuracy: The accuracy of the resistance ratio measurement depends also on the SQUID feedback accuracy in canceling the total ampere-turns' number, i.e., in setting the current ratio $r_I = I_S/I_P$ to the target ratio given by (1). A setpoint error comes from the finite value of the open-loop gain G_{OLG} of the SQUID electronics and the imperfect adjustment of the current ratio prior to the SQUID feedback operation. A type B relative uncertainty, u_B^{FB}, lower than 10^{-11} is determined for the usual prior adjustment level of the current ratio (see Appendix D).

2) Leakage Current to Ground: Several experiments were carried out to estimate the impact of leakage current to ground on the measurement accuracy. No leakage current could be unveiled by comparing measurements of the resistance ratios 100 $\Omega/(R_K/2)$ and 200 $\Omega/(R_K/2)$, performed with the ground either connected in position A (I_g parallel to R_S) or position B (I_g fully deviated) since no significant deviation was found within a relative uncertainty of about 0.8×10^{-9}. Comparisons were, therefore, repeated with a larger secondary resistance $R_S = 1$ kΩ to amplify the effect of leakage currents and make it detectable. From the comparison of the two measurements of the 1 k$\Omega/1$ kΩ ratio performed with the resistors interchanged, a relative deviation of $(-3 \pm 0.4) \times 10^{-9}$ is found for the measurement of one resistance ratio for the ground in position A, which reduces to $(-0.04 \pm 0.3) \times 10^{-9}$ for the ground in

Ratio	100 $\Omega/(R_K/2)$	100 $\Omega/10$ $k\Omega$
Relative deviation	$(-1.4 \pm 1.5) \times 10^{-9}$	$(-0.7 \pm 1.4) \times 10^{-9}$

position B. A similar relative deviation of a few 10^{-9} is also found by comparing the measurements of the 1-k$\Omega/(R_K/2)$ ratio obtained for both ground positions. One concludes that a significant negative discrepancy of a few 10^{-9} resulting from leakage currents exists but can, nevertheless, be fully canceled by moving the ground in position B. From these comparisons, a Type B relative uncertainty, u_B^g, of about 0.5×10^{-9}, i.e., ten times lower, can, therefore, be deduced for the measurement of the 100-$\Omega/(R_K/2)$ ratio with the ground in position A. It falls below 0.1×10^{-9} by connecting the ground in position B. Let us remark that further characterizations are required to explain the origin of the larger than expected leakage current to ground. Indeed, its magnitude cannot be directly explained from the value of the leakage resistance to the ground of the whole measurement system (bridge, CCC, and resistance standards), which is measured to be higher than 4 TΩ. Moreover, the leakage resistance to the ground of the current sources alone is higher than 80 TΩ confirming the high galvanic insulation of the operational amplifiers.

3) Small Contributions: No significant effect of the current reversal duration (from I^+ to I^- and reversely) was found within a relative uncertainty of 0.35×10^{-9} by varying its value from 12 to 24 s while keeping the same acquisition time. The absence of observable asymmetry of the voltage deviations measured by the ND for I^+ and I^- current directions indicates a small effect of noise rectification in the measurements discussed. However, further work is required to generalize this conclusion to any ratio measurement.

To conclude, the total type B relative uncertainty is estimated to be either 0.7×10^{-9} or 0.5×10^{-9} depending on whether the ground is connected to position A or B. The type A uncertainty being much smaller, the standard combined relative uncertainty, u_c, is significantly below 10^{-9}. Further reduction of the measurement uncertainty will come from the improvement of the current divider calibration.

D. Validation of Measurement Performance

Table IV reports on the deviations between the measurements of the 100 $\Omega/(R_K/2)$ and 100 $\Omega/10$ kΩ ratios performed using the new and the old bridges. It shows that there is no significant discrepancy within a combined relative uncertainty below 1.5×10^{-9}. Let us note that the comparison uncertainty is limited by the larger type A uncertainty of the older bridge. This agreement between the two RBs, which differ not only by their electronics but also by their CCC and SCD, make us very confident in our measurements of these resistance ratios. It consolidates the uncertainty budget described previously in Table III.

Moreover, the measured value of the 100-$\Omega/(R_K/2)$ ratio and the ratio value deduced by combining the measurements of the 1-k$\Omega/(R_K/2)$ and 100-$\Omega/1$ kΩ ratios are found

in agreement within a relative uncertainty of 1.2×10^{-9} (with the ground in position B). This consistency check confirms the small impact of the leakage current in position B of the ground and that the 10^{-9} relative uncertainty also applies to the measurement of other resistance ratios than 100 $\Omega/(R_K/2)$.

Besides, the new LNE bridge was used to perform accurate universality tests of the QHE [6], [32]. The agreement of the quantized Hall resistance, R_H, measured in GaAs and graphene devices was demonstrated with a record [6] relative uncertainty of 8×10^{-11}. This result was obtained by comparing the two measurements of the 100-$\Omega/(R_H/2)$ ratio carried out using a 100-Ω transfer resistor. This performance, therefore, emphasizes the low-noise level and the reproducibility of the measurement bridge, rather than its accuracy since many Type B uncertainty contributions are canceled by the design of the comparison protocol. The capability of the RB to perform measurements at low frequency (2 Hz) allowed the determination of the temperature evolution of the quantized Hall resistance in graphene during dynamic temperature drift [32]. Finally, many elements of the RB, i.e., the CCC, the current source, and the current divider, were also used to build the programmable quantum current generator that allowed a practical realization of the ampere from the elementary charge with a 10^{-8} relative uncertainty [33].

VIII. CONCLUSION

A new comparison RB based on a CCC was built at LNE. It is based on low-noise synchronized current sources, a new CCC with a very low-noise level of 80 pA.t/Hz$^{1/2}$, a SCD characterized by one-year stability of the fractions within the calibration uncertainty of 0.3×10^{-9}, and also a QCD that cancels voltage overshoots during current transitions. Accurate measurements of the resistance ratios, 100 $\Omega/(R_K/2)$, 100 $\Omega/10$ kΩ, 200 $\Omega/(R_K/2)$, 1 k$\Omega/1$ kΩ, 1 k$\Omega/(R_K/2)$, and 100 $\Omega/1$ kΩ, were achieved. Besides, stable operation of the RB was also demonstrated for the measurement not only of the 10-k$\Omega/1$-MΩ ratio but also of the 1-$\Omega/100$-Ω ratio (with current dividers inserted in the primary circuit). Next work will report on the measurement accuracy of these two resistance ratios.

The 100-$\Omega/(R_K/2)$ ratio can be measured with a type A relative uncertainty below 0.2×10^{-9} within 1-h measurement time. This performance results not only from the lower noise of the bridge but also from the optimization of the data acquisition thanks to the QCD. Further improvement would require a lower-noise ND than the EM N11. The total type B relative uncertainty, estimated considering main contributions, is of 0.5×10^{-9}. This leads to a standard combined relative uncertainty of only 0.6×10^{-9}. A slightly smaller combined standard uncertainty is expected at term by implementing a new calibration method of the SCD.

APPENDIX A
CCC CALCULATIONS

The sensitivity of the CCC, S_{CCC}, depends on the number of turns N_{PC} of the pickup coil coupled to the CCC through
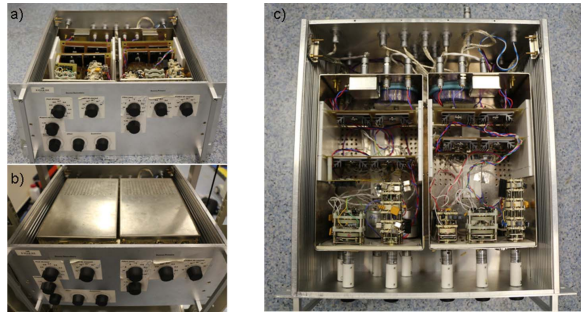
Fig. 15.   Pictures of (a) and (b) primary and (c) secondary current sources, each one being placed in an independent box.

the relationship

$$S_{\mathrm{CCC}} = (2/k) N_{\mathrm{PC}} S_{\mathrm{SQ}} \tag{8}$$

where k is the coupling constant between the CCC and the pickup coil, and S_{SQ} is the SQUID sensitivity (in $\mu\mathrm{A}/\phi_0$). The best sensitivity $S_{\mathrm{CCC}}^{\mathrm{opt}}$ is obtained for $N_{\mathrm{PC}}^{\mathrm{opt}}$ given by

$$N_{\mathrm{PC}}^{\mathrm{opt}} = \sqrt{L_i / L_{\mathrm{CCC}}^{\mathrm{eff}}} \tag{9}$$

where $L_{\mathrm{CCC}}^{\mathrm{eff}}$ is the effective self-inductance of the CCC taking into account the proximity of the superconducting screen that isolates the SQUID from external magnetic fields (Earth's field for instance). $L_{\mathrm{CCC}}^{\mathrm{eff}}$ and, therefore, S_{CCC} can be determined in a given geometry using the analytical calculation of Sesé and coauthors [24], [25]. In our case, one calculates $L_{\mathrm{CCC}}^{\mathrm{eff}} \sim 14$ nH, $N_{\mathrm{PC}}^{\mathrm{opt}} = 12$, and $S_{\mathrm{CCC}}^{\mathrm{opt}} = 5\ \mu\mathrm{A.t}/\phi_0$. Due to geometrical constraints, the number of turns of the pickup coil was reduced to $N_{\mathrm{PC}} = 6$, leading to an experimental sensitivity $S_{\mathrm{CCC}} = 8\ \mu\mathrm{A.t}/\phi_0$ close to the calculated value of $6\ \mu\mathrm{A.t}/\phi_0$.

APPENDIX B
CURRENT SOURCES

A. Implementation of the Electronic Circuits

Electronic circuits of each current source are integrated but electrically isolated with PTFE material, into their own metallic box connected to ground, as shown in pictures of Fig. 15. The electronic components are powered by stabilized voltages provided by a circuit itself energized by rechargeable batteries placed in their own metallic box (see Fig. 9).

The only electrical link existing between the electronic circuits and the ground comes from the insulation differential amplifiers. Those that are used to probe the external piloting voltage and the SQUID feedback voltage are based on OPA128LM precision operational amplifiers (in combination with OPA97 devices) that ensure a high-isolation resistance (in principle, $\sim 10^{15}\ \Omega$). All these precautions aim at canceling leakage currents. Let us note that these amplifiers are characterized by a large voltage noise at low frequencies ($4\ \mu\mathrm{V_{p-p}}$ between 0.1 and 10 Hz), but the current ratio is not sensitive to it by construction. On the other hand, it is sensitive to the noise of the insulation differential amplifier at the entry of the secondary current source used to probe the

TABLE V
RESISTANCE AND CAPACITANCE VALUES IN THE LAST STAGE OF THE SECONDARY CURRENT SOURCE FOR THE DIFFERENT CURRENT RANGES

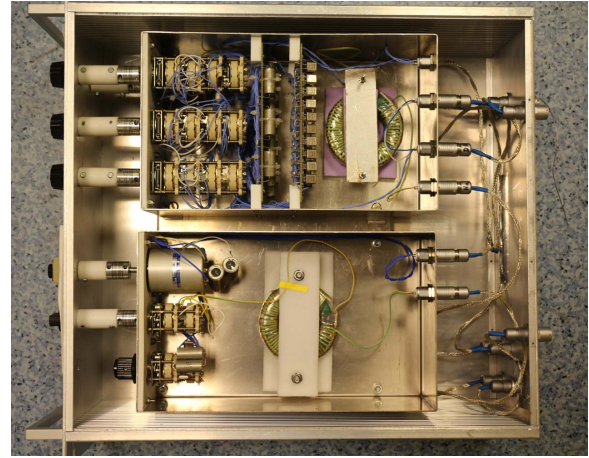| Range	R_{C}	R_{E}	C_{F}	R_{F}
1 μA	5 MΩ	1 MΩ	300 pF	4 MΩ
10 μA	500 kΩ	100 kΩ	300 pF	400 kΩ
100 μA	50 kΩ	10 kΩ	3 nF	40 kΩ
1 mA	5 kΩ	1 kΩ	30 nF	4 kΩ
10 mA	500 Ω	100 Ω	300 nF	400 Ω
100 mA	50 Ω	10 Ω	3 μF	40 Ω

Fig. 16.   Pictures of the SCD (top) and of the QCD (bottom), each one being placed in an independent box.

voltage after the low-pass filter of the primary current source. Here, precision OPA111BM operational amplifiers with a lower voltage noise ($1.2\ \mu\mathrm{V_{p-p}}$ between 0.1 and 10 Hz) are used to optimize the current ratio stability at the expense of a reduction of the isolation resistance (in principle $\sim 10^{13}\ \Omega$).

B. Passive Components of the Secondary Current Circuit

See Table V.

APPENDIX C
CURRENT DIVIDERS

Fig. 16 shows a picture of the SCD and of the QCD.

A. SCD Calibration

A fraction of the SCD is calibrated from the measurement of the ratio $V_{\mathrm{ab}}/V_{\mathrm{ref}}$, where V_{ab} is the low voltage, indicated in Fig. 7 and measured using an HP34420A nanovoltmeter (1-mV range), and V_{ref} is the reference voltage of a 10-V Zener standard, which is applied in place of the auxiliary winding N_{A}. To reduce the measurement uncertainty, the range of the HP34420A nanovoltmeter used (1 mV) is calibrated from the V_{ref} voltage reference just before and after the $V_{\mathrm{ab}}/V_{\mathrm{ref}}$ measurements. This is achieved by generating a calibrated 1-mV voltage from $V_{\mathrm{ref}} = 10$ V using series and parallel implementations of two ESI SR1010 transfer resistance standards (made of 1-kΩ and 10-Ω resistors, respectively). The excellent linearity of the HP34420A nanovoltmeter allows the calibration of 1-mV range by the

measurement of the 1-mV value only. This method allows the calibration of any fraction between 0 and 5×10^{-5} with an upper bound uncertainty of 0.3×10^{-9}.

B. QCD Calculations

Let us consider stray capacitances C_P and C_S in parallel to the resistors R_P and R_S. The voltage balance equation is given by

$$\frac{R_P}{1 + j R_P C_P \omega} I_P - \frac{R_S}{1 + j R_S C_S \omega} I_S = 0. \tag{10}$$

Using the ampere-turn balance equation (3) leads to

$$\left[R_P(N_S + \epsilon_{\mathrm{eq}} N_A) - R_S N_P - R_P R_S \epsilon_{\mathrm{eq}}^{\mathrm{q}} N_A^{\mathrm{q}} \omega^2 \right]$$
$$+ j\omega R_P \left[R_S(N_S + \epsilon_{\mathrm{eq}} N_A) - R_S N_P C_P - \epsilon_{\mathrm{eq}}^{\mathrm{q}} N_A^{\mathrm{q}} \right] = 0. \tag{11}$$

First-order approximation in ω applied to both the real and imaginary parts of the equation leads to (2) and (4).

APPENDIX D
ESTIMATION OF THE SQUID FEEDBACK ACCURACY

Although the SQUID amplifier is based on an integrator that leads to an infinite gain at dc, measurements are, in practice, carried out with a finite time periodicity of the current reversal, typically of 70 s. This causes a relative current ratio error, which is equal to $(\Delta^{\mathrm{Prior-adj}} r_I / r_I) \times (G_{\mathrm{CLG}} / G_{\mathrm{OLG}})$, where $\Delta^{\mathrm{Prior-adj}} r_I / r_I$ is the relative deviation between the target ratio and the preliminary current ratio as it is adjusted prior to the SQUID feedback operation. Measurements of the 100-$\Omega/(R_K/2)$ resistance ratio were performed for $\Delta^{\mathrm{Prior-adj}} r_I / r_I$ values as large as a few $\pm 10^{-4}$. From the discrepancies measured, a relative error in the measurement of the resistance ratio lower than 10^{-11} is deduced for the usual adjustment of the current ratio, i.e., for $\Delta^{\mathrm{Prior-adj}} r_I / r_I \sim 2 \times 10^{-6}$ (as discussed in Section IV-B). This corresponds to a value $G_{\mathrm{OLG}} > 7.5 \times 10^4$ V/ϕ_0, compatible with that determined in quantized current experiment [33].

ACKNOWLEDGMENT

REFERENCES

[1] (2019). *The International System of Units (SI)*. [Online]. Available: https://www.bipm.org/en/measurement-units/

[2] (2019). *Mise en Pratique for Definition Ampere Other Electric Units SI*. SI Brochure-9th edition (2019)-Appendix 2. [Online]. Available: https://www.bipm.org/utils/en/pdf/si-mep/SI-App2-ampere.pdf

[3] W. Poirier, S. Djordjevic, F. Schopfer, and O. Thevenot, "The ampere and the electrical units in the quantum era," *Comp. Rendus Phys.*, vol. 20, pp. 92–128, Jan./Feb. 2019.

[4] B. Jeckelmann and B. Jeanneret, "The quantum Hall effect as an electrical resistance standard," *Rep. Prog. Phys.*, vol. 64, no. 12, p. 1603, 2001.

[5] W. Poirier and F. Schopfer, "Resistance metrology based on the quantum Hall effect," *Eur. Phys. J. Special Topics*, vol. 172, pp. 207–245, Jun. 2009.

[6] R. Ribeiro-Palau *et al.*, "Quantum Hall resistance standard in graphene devices under relaxed experimental conditions," *Nature Nanotechnol.*, vol. 10, no. 11, pp. 965–971, Nov. 2015.

[7] I. K. Harvey, "A precise low temperature DC ratio transformer," *Rev. Sci. Instrum.*, vol. 43, no. 11, pp. 1626–1629, Nov. 1972.

[8] J. Gallop and F. Piquemal, *Squid Handbook*, vol. 2, J. Clarke and A. I. Braginski, Eds. Weinheim, Germany: Wiley, 2006, pp. 95–137.

[9] F. Delahaye and D. Reymann, "Progress in resistance ratio measurements using a cryogenic current comparator at LCIE," *IEEE Trans. Instrum. Meas.*, vol. 34, no. 2, pp. 316–319, Jun. 1985.

[10] J. M. Williams and A. Hartland, "An automated cryogenic current comparator resistance ratio bridge," *IEEE Trans. Instrum. Meas.*, vol. 40, no. 2, pp. 267–270, Apr. 1991.

[11] A. Hartland, "The quantum Hall effect and resistance standards," *Metrologia*, vol. 29, no. 2, pp. 175–190, Jan. 1992.

[12] R. F. Dziuba and R. E. Elmquist, "Improvements in resistance scaling at NIST using cryogenic current comparators," *IEEE Trans. Instrum. Meas.*, vol. 42, no. 2, pp. 126–130, Apr. 1993.

[13] F. Delahaye, T. Witt, F. Piquemal, and G. Genevès, "Comparison of quantum Hall effect resistance standards of the BNM/LCIE and the BIPM," *IEEE Trans. Instrum. Meas.*, vol. 44, no. 2, pp. 258–261, Apr. 1995.

[14] F. Delahaye, "An AC-bridge for low-frequency measurements of the quantized Hall resistance," *IEEE Trans. Instrum. Meas.*, vol. 40, no. 6, pp. 883–888, Dec. 1991.

[15] H. Seppa and A. Satrapinski, "AC resistance bridge based on the cryogenic current comparator," *IEEE Trans. Instrum. Meas.*, vol. 46, no. 2, pp. 463–466, Apr. 1997.

[16] F. Delahaye and D. Bournaud, "Accurate AC measurements of standard resistors between 1 and 20 Hz," *IEEE Trans. Instrum. Meas.*, vol. 42, no. 2, pp. 287–291, Apr. 1993.

[17] A. Satrapinski, M. Götz, E. Pesel, N. Fletcher, P. Gournay, and B. Rolland, "New generation of low-frequency current comparators operated at room temperature," *IEEE Trans. Instrum. Meas.*, vol. 66, no. 6, pp. 1417–1424, Jun. 2017.

[18] C. A. Sanchez, B. M. Wood, and A. D. Inglis, "CCC bridge with digitally controlled current sources," *IEEE Trans. Instrum. Meas.*, vol. 58, no. 4, pp. 1202–1205, Apr. 2009.

[19] D. Drung *et al.*, "Improving the stability of cryogenic current comparator setups," *Superconductor Sci. Technol.*, vol. 22, no. 11, Nov. 2009, Art. no. 114004.

[20] M. Götz *et al.*, "Improved cryogenic current comparator setup with digital current sources," *IEEE Trans. Instrum. Meas.*, vol. 58, no. 4, pp. 1176–1182, Apr. 2009.

[21] J. M. Williams, T. J. B. M. Janssen, G. Rietveld, and E. Houtzager, "An automated cryogenic current comparator resistance ratio bridge for routine resistance measurements," *Metrologia*, vol. 47, no. 3, p. 167, Mar. 2010.

[22] BIPM. (2019). *The BIPM Key Comparison Database (KCDB), Key and Supplementary Comparisons (Appendix b), Comparison BIPM.em-k12*. [Online]. Available: https://kcdb.bipm.org

[23] L. Soukiassian, G. Spengler, D. Leprat, F. Schopfer, and W. Poirier, "New cryogenic current comparator-based resistance comparison bridge at LNE," in *Proc. CPEM*, Daejeon, South Korea, Y. S. Song and J.-S. Kang, Eds. Piscataway, NJ, USA: IEEE Press, Jun. 2010, p. 761, doi: 10.1109/CPEM.2010.5544176.

[24] J. Sese, F. Lera, A. Camon, and C. Rillo, "Calculation of effective inductances of superconducting devices. Application to the cryogenic current comparator," *IEEE Trans. Appiled Supercond.*, vol. 9, no. 1, pp. 58–62, Mar. 1999.

[25] J. Sese, E. Bartolome, J. Flokstra, G. Rietveld, A. Camon, and C. Rillo, "Simplified calculus for the design of a cryogenic current comparator," *IEEE Trans. Instrum. Meas.*, vol. 52, no. 2, pp. 612–616, Apr. 2003.

[26] J. Gallop and F. Piquemal, *SQUIDs for Standards Metrology* (Applications of SQUIDs and SQUID Systems), vol. 2. Berlin, Germany: Wiley, 2006, pp. 95–137.

[27] S. Awan, B. Kibble, and J. Schurr, *Coaxial Electrical Circuits for Interference-Free Measurements*. New York, NY, USA: The Institution of Engineering and Technology, 2011.

[28] D. Drung, M. Götz, E. Pesel, H. J. Barthelmess, and C. Hinnrichs, "Aspects of application and calibration of a binary compensation unit for cryogenic current comparator setups," *IEEE Trans. Instrum. Meas.*, vol. 62, no. 10, pp. 2820–2827, Oct. 2013.

[29] M. Götz and D. Drung, "Stability and performance of the binary compensation unit for cryogenic current comparator bridges," *IEEE Trans. Instrum. Meas.*, vol. 66, no. 6, pp. 1467–1474, Jun. 2017.

[30] D. Allan, "Should the classical variance be used as a basic measure in standards metrology?" *IEEE Trans. Instrum. Meas.*, vol. 36, no. 2, pp. 646–654, Jun. 1987.

[31] T. Witt, "Allan variances and spectral densities for DC voltage measurements with polarity reversals," *IEEE Trans. Instrum. Meas.*, vol. 54, no. 2, pp. 550–553, Apr. 2005.

[32] F. Lafont *et al.*, "Quantum Hall resistance standards from graphene grown by chemical vapour deposition on silicon carbide," *Nature Commun.*, vol. 6, no. 1, p. 6806, Nov. 2015.

[33] J. Brun-Picard, S. Djordjevic, D. Leprat, F. Schopfer, and W. Poirier, "Practical quantum realization of the ampere from the elementary charge," *Phys. Rev. X*, vol. 6, no. 4, Dec. 2016, Art. no. 041051.

Dominique Leprat was a Technician with the Electrical Metrology Department, Laboratoire national de métrologie et d'essais (LNE), Trappes, France, from 2001 to 2017. He was first involved in the activity of traceability of alternating voltage based on thermal transfer. In 2007, he joined the quantum Hall effect team to develop metrology instrumentation.

Wilfrid Poirier graduated from the Ecole Supérieure de Physique et de Chimie Industrielles de Paris (ESPCI), Paris, France, in 1993. He received the Ph.D. degree in solid-state physics from CEA-SPEC, Saclay, France, in 1997 and the Habilitation to Direct Research from the University of Paris-SUD, Orsay, France, in 2017.

He completed his thesis on quantum electronic transport at the CEA-SPEC. He joined LCIE, Fontenay-aux-Roses, France, in 1998 and then the Laboratoire national de métrologie et d'essais (LNE), Trappes, France, in 2001, as the Head of studies on quantum resistance standards. Since then, he has devoted his research to quantum electrical metrology. These included the development of a graphene quantum resistance standard, of GaAs-based quantum Hall arrays and the realization of universality tests of the quantum Hall effect. He has also been involved in the development of precision quantum instrumentation based on Superconducting QUantum Interference Device (SQUID) technology. More recently, he has proposed and developed a quantum current generator to achieve the new definition of ampere.

Félicien Schopfer received the Engineer's degree from the École Nationale Supérieure de Physique—Grenoble INP, Grenoble, France, in 2001, the master's degree in condensed matter physics from the University of Grenoble, Grenoble, in 2001, and the Ph.D. degree in physics from the University of Grenoble, Grenoble, in 2005 for quantum electronic transport experiments in nanostructures carried out at CNRS, Grenoble, France.

He was appointed at the Laboratoire national de métrologie et d'essais (LNE), Trappes, France, in 2005, to advance research in quantum electrical metrology. His research has mainly focused on the quantum Hall effect (QHE) for applications in fundamental metrology. He worked on quantum Hall arrays in GaAs/AlGaAs, coauthored reproducibility and universality tests of the quantum Hall effect with record uncertainties, and is strongly involved in graphene research, notably with important results for the development of the quantum Hall resistance standard operating under relaxed experimental conditions.